# Iron Oxide Decorated MoS$_2$ Nanosheets with Double PEGylation for Chelator-Free Radiolabeling and Multimodal Imaging Guided Photothermal Therapy

Teng Liu,[†] Sixiang Shi,[‡] Chao Liang,[†] Sida Shen,[†] Liang Cheng,[†] Chao Wang,[†] Xuejiao Song,[†] Shreya Goel,[‡] Todd E. Barnhart,[§] Weibo Cai,[*,‡,§,‖,⊥] and Zhuang Liu[*,†]

[†]Institute of Functional Nano & Soft Materials (FUNSOM), Collaborative Innovation Center of Suzhou Nano Science and Technology, the Jiangsu Key Laboratory for Carbon-Based Functional Materials & Devices, Soochow University, Suzhou, Jiangsu 215123, China, [‡]Materials Science Program, [§]Department of Medical Physics, and [‖]Department of Radiology, University of Wisconsin—Madison, Madison, Wisconsin, United States, and [⊥]University of Wisconsin Carbone Cancer Center, Madison, Wisconsin, United States

ABSTRACT Theranostics for *in vivo* cancer diagnosis and treatment generally requires well-designed nanoscale platforms with multiple integrated functionalities. In this study, we uncover that functionalized iron oxide nanoparticles (IONPs) could be self-assembled on the surface of two-dimensional MoS$_2$ nanosheets *via* sulfur chemistry, forming MoS$_2$-IO nanocomposites, which are then modified with two types of polyethylene glycol (PEG) to acquire enhanced stability in physiological environments. Interestingly, ^{64}Cu, a commonly used positron-emitting radioisotope, could be firmly adsorbed on the surface of MoS$_2$ without the need of chelating molecules, to enable *in vivo* positron emission tomography (PET) imaging. On the other hand, the strong near-infrared (NIR) and superparamagnetism of MoS$_2$-IO-PEG could also be utilized for photoacoustic tomography (PAT) and magnetic resonance (MR) imaging, respectively. Under the guidance by such triple-modal imaging, which uncovers efficient tumor retention of MoS$_2$-IO-(d)PEG upon intravenous injection, *in vivo* photothermal therapy is finally conducted, achieving effective tumor ablation in an animal tumor model. Our study highlights the promise of constructing multifunctional theranostic nanocomposites based on 2D transitional metal dichalcogenides for multimodal imaging-guided cancer therapy.
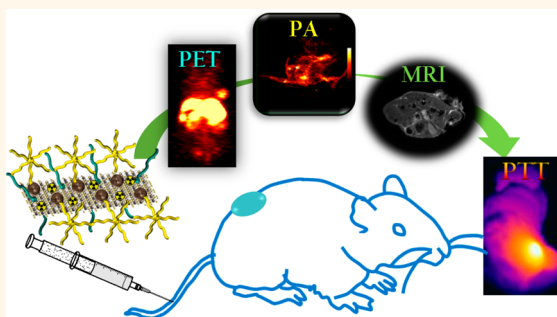
KEYWORDS: MoS$_2$ nanosheets · iron oxide nanoparticles · chelate-free ^{64}Cu labeling · multimodal imaging · photothermal therapy

Since the discovery of graphene, ultrathin two-dimensional (2D) nanomaterials have attracted tremendous interest due to their unique structures and properties.[1] Recently, transitional metal dichalcogenides (TMDCs) have emerged as a next-generation 2D material alternative to graphene.[2,3] Besides many intriguing properties similar to those of graphene, TMDCs nanosheets on the other hand have abundant elemental compositions, which enable more precise tuning of their physical and chemical properties, an advantage over graphene.[4] Therefore, in the past several years there have been numerous reports exploring the applications of TMDCs as electronic devices,[5] transistors,[6,7] energy storage materials,[8,9] and catalysts.[10,11] Recently, a few groups including ours have found that atomically thin TMDC nanosheets are also promising in the biomedical field. Chou *et al.* discovered that sulfur-terminated molecules could be used to modify MoS$_2$ nanosheets to acquire better physiological stability and biocompatibility.[12] Applying their high absorbance in the near-infrared (NIR) region, MoS$_2$,[13] WS$_2$,[14] and Bi$_2$Se$_3$[15] nanosheets have been utilized in photothermal therapy (PTT) of cancers. Taking advantage of the large surface area attributed to the 2D structure, MoS$_2$-based biosensors[16] and drug delivery

systems[17,18] have been developed. However, there is still much room to develop TMDC-based nanoscale platforms, particularly to integrate TMDCs with other functional nanostructures, for applications in cancer theranostics.

To realize personalized medicine, optimize therapeutic efficiency, and monitor therapeutic responses, imaging before, during, and after therapy has been playing increasingly important roles to guide the planning of treatment for individual patients.[19−21] However, each single imaging modality usually would have its inherent limitations, such as limited tissue penetration in optical imaging, relatively low sensitivity in magnetic resonance imaging, and the absence of anatomy information in nuclear imaging. Multimodal imaging, which is able to compensate for inherent limitations of each single imaging modality, has thus been an important trend in the development of new biomedical imaging instruments[22] and contrasting agents.[23−26] Therefore, nanoscale theranostic platforms[27−30] with highly integrated imaging and therapy functionalities are of great interest in biomedicine nowadays.

Motivated by the above needs, we developed a multifunctional TMDC-based nanoplatform for multimodal imaging-guided photothermal therapy of cancer. It was found that meso-2,3-dimercaptosuccinnic acid (DMSA)-modified iron oxide nanoparticles (IONPs) could self-assemble on the surface of atomically thin MoS_2 nanosheets, likely via sulfur chemistry occurring on the defect sites of MoS_2. Subsequently, the obtained MoS_2-IO nanocomposites were simultaneously functionalized by lipoic acid terminated polyethylene glycol (LA-PEG), which is anchored on MoS_2, and amino-terminated six-arm PEG, which is conjugated to IONPs (Figure 1a). Such double-PEGylated MoS_2-IO (MoS_2-IO-(d)PEG) exhibited great stability in physiological environments in the presence of glutathione. Intriguingly, without the need of chelating agents, MoS_2-IO-(d)PEG could be efficiently labeled by a ^{64}Cu radioisotope with high labeling yield (∼70%) and great stability. Utilizing ^{64}Cu-labeled nanocomposites, which also exhibit high near-infrared (NIR) absorbance attributed to MoS_2 nanosheets and a strong superparamagnetic property offered by decorated IONPs, triple-modal positron emission tomography (PET), photoacoustic tomography (PAT), and magnetic resonance (MR) imaging were conducted in tumor-bearing mice, revealing efficient tumor accumulation of nanocomposites. Guided by the imaging results, photothermal therapy was finally carried out, achieving complete ablation of 4T1 murine breast tumors under 808 nm laser irradiation. Our work presents a facile design to incorporate many different functionalities into one single theranostic nanoplatform based on TMDCs, which is promising for future biomedical applications.

RESULTS AND DISCUSSIONS

Single-layered MoS_2 nanosheets were synthesized by the Morrison method,[31] a commonly adopted method to exfoliate TMDCs on a large scale. Typically, bulk MoS_2 was inserted by n-butyllithium in hexane under protection of N_2 in a glovebox. After removing excess lithium and hexane, the precipitate was taken out, sonicated in water, and then washed via centrifugation and dialysis to obtain water-soluble single-layered MoS_2 nanosheets. As revealed by transmission electron microscopy (TEM) (Figure 1b), as-made MoS_2 nanosheets were mostly single-layer sheets with sizes in the range 50−200 nm. X-ray diffraction (XRD) data indicated the hexagonal structure for MoS_2 (Supporting Figure S1a), consistent with those described in previous reports.[12,32] The high-resolution TEM (HRTEM) imaging (Supporting Figure S1b) revealed the lattice spacing of MoS_2 nanosheets to be 2.1 Å, which could be assigned to the (006) planes of the hexagonal structure formed by Mo and S atoms.

During drastic intercalation and exfoliation, some of the sulfur atoms would be lost from the sandwich surface of MoS_2 nanosheets, forming defects available for binding by sulfur-terminated molecules.[12] IONPs synthesized by the classical thermo-decomposition method and functionalized with DMSA were then mixed with as-made MoS_2 nanosheets under ultrasonication. Although both negatively charged (Supporting Figure S2a), DMSA-modified IONPs could self-assemble on the MoS_2 surface as a well-controlled single-particle layer, owing to the binding of thiol groups on DMSA-coated IONPs to the defect sites on MoS_2 nanosheets. In contrast, dopamine-modified IONPs with positive surface charges would aggregate with MoS_2 nanosheets via electrostatic attraction, forming irregular agglomerates (Supporting Figure S2b). As the mass ratio of MoS_2 to DMSA-IONPs nanosheets varied from 1:2 to 1:10, IONPs gradually occupied the surface of MoS_2 nanosheets until saturation (Figure 1b). MoS_2-IO composites obtained with a feeding ratio of 1:5 (mass ratio of MoS_2 to IONPs), at which condition the majority of the MoS_2 surface was covered by IONPs, were chosen for further experiments. The elemental mapping of molybdenum, sulfur, iron, and oxygen by energy-dispersive X-ray spectroscopy (EDS) under scanning transmission electron microscopy (STEM) further revealed that IONPs were homogeneously distributed on the surface of MoS_2 nanosheets (Figure 1c). The exact MoS_2:IONPs mass ratio in the final product was measured by inductively coupled plasma atomic emission spectroscopy (ICP-AES) to be 1:6.4. Compared with previously reported methods to synthesize TMDC−nanoparticle composites in which Au, Ag, Pd,[33] or Fe_3O_4 nanoparticles[34] were directly grown on the surface of TMDC nanosheets, our method relying on the self-assembly of premade
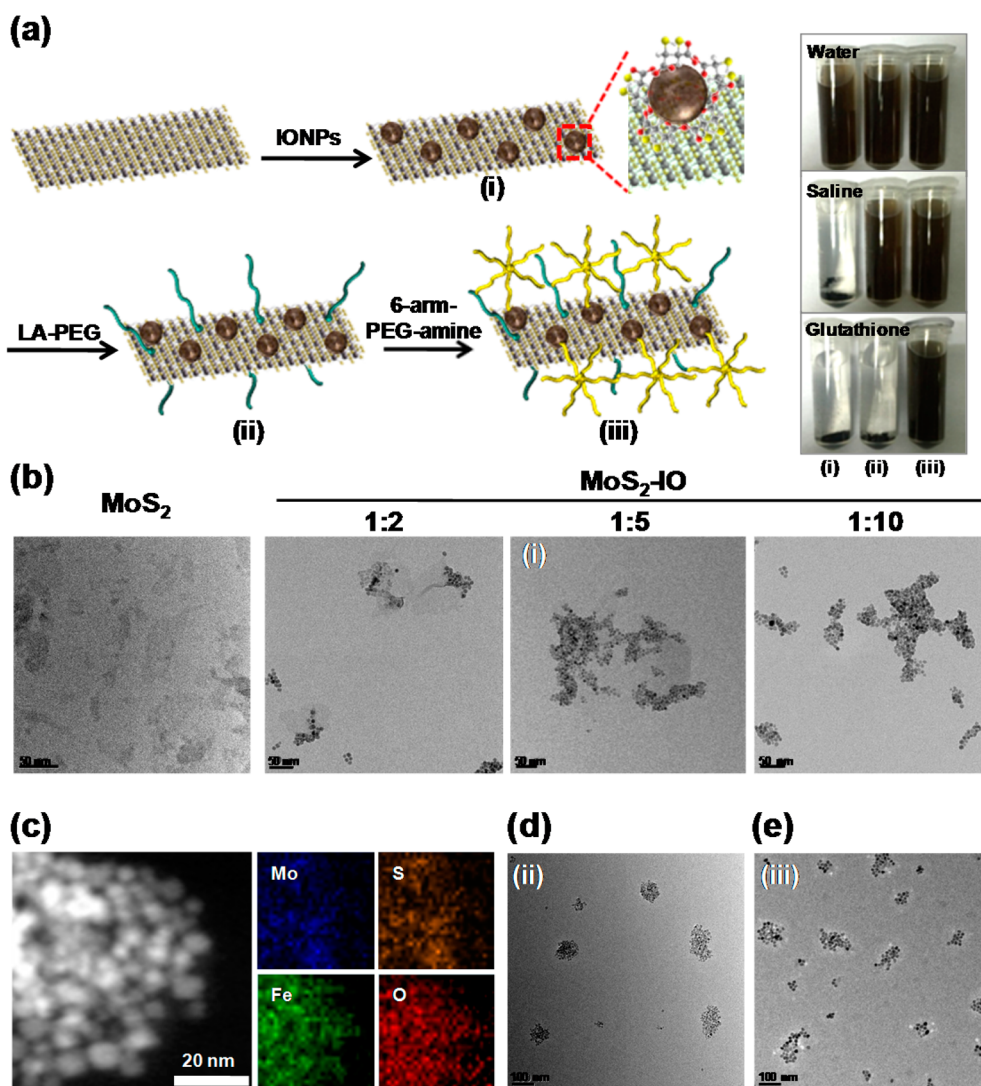
Figure 1. Synthesis and characterization of MoS₂-IO nanocomposites with or without PEG. (a) Schematic presentation to illustrate the self-assembly of DMSA-modified IONPs on exfoliated MoS₂ nanosheets and the subsequent PEGylation. Inset photos: Photographs of MoS2-IO (i), MoS2-IO-(s)PEG (ii), and MoS2-IO-(d)PEG (iii) in water, saline (0.9 wt %), and glutathione (0.3 wt %) solution after 24 h. **(b)** TEM images of MoS₂ nanosheets and MoS₂-IO nanocomposites with different feeding mass ratios (MoS₂:IO = 1:2, 1:5, 1:10). **(c)** STEM image and EDS elemental maps of MoS₂-IO. **(d, e)** TEM images of single-PEGylated MoS₂-IO (MoS₂-IO-(s)PEG (ii)) (d) and double-PEGylated MoS₂-IO (MoS₂-IO-(d)PEG (iii)) (e).

high-quality nanoparticles synthesized by the state-of-the-art method on the surface of TMDCs is a rather easy and controllable approach.

Although soluble in water, MoS₂-IO would quickly aggregate and precipitate in the presence of salts (Figure 1a). Next, to enhance the stability of our nanocomposite in physiological solutions to enable further biomedical applications, thiolated polymer LA-PEG was adopted to modify MoS₂-IO the same way PEGylated WS₂[14] or MoS₂[17,18] nanosheets are prepared (Figure 1a,d). After stirring overnight, the disulfide group of LA-PEG was strongly bonded to the defect site on MoS₂, obtaining MoS₂-IO-(s)PEG with great stability in saline (Figure 1a, inset). However, different from as-made MoS₂, the number of surface defects reactive to LA-PEG in the MoS₂-IO composite should be lower due to occupation of IONPs on the surface of

MoS₂ nanosheets, reducing PEGylation efficiency. In the presence of glutathione, a thiol-containing molecule widely found in physiological environments, such MoS₂-IO-(s)PEG showed obviously reduced stability owing to the replacement of LA-PEG by glutathione (Figure 1a, inset). To further improve the physiological stability of our nanocomposite, amine-terminated branched PEG was then conjugated to the carboxyl groups on the IONP surface *via* amide formation. The obtained MoS₂ with double PEGylation (MoS₂-IO-(d)PEG) showed the same uniform single-particle-layer structure (Figure 1e) with slightly larger hydrodynamic size compared to MoS₂-IO-(s)PEG (Supporting Figure S2d). Due to the enhancement in PEGylation efficiency (Supporting Figure S4a), MoS₂-IO-(d)PEG exhibited excellent stability in the saline solution containing glutathione (Figure 1a, inset). In addition, although
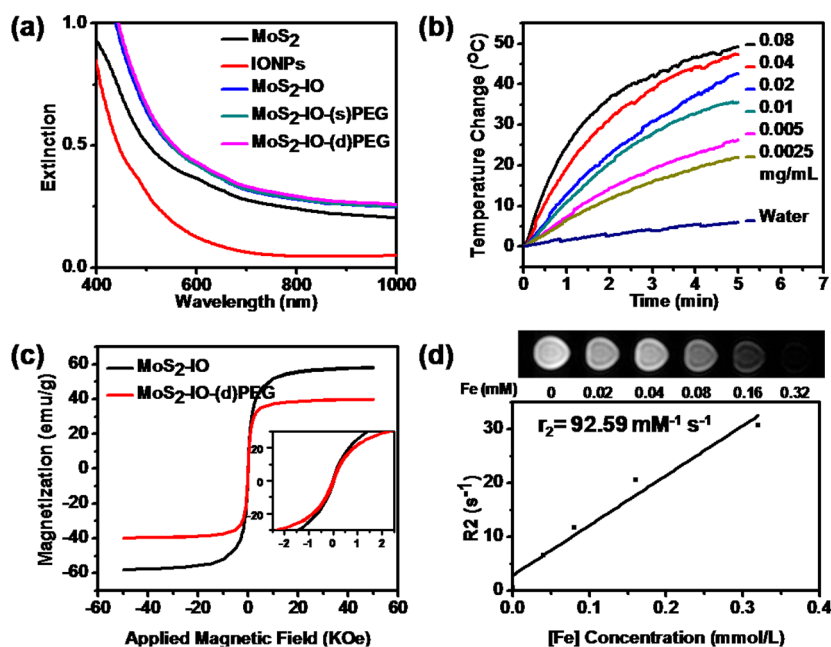
Figure 2. Optic and magnetic characterization of MoS$_2$-IO-(d)PEG. (a) UV−vis−NIR spectra of MoS$_2$ nanosheets, DMSA-modified IONPs, MoS$_2$-IO, MoS$_2$-IO-(s)PEG, and MoS$_2$-IO-(d)PEG in aqueous solutions ([MoS$_2$] = 8.2 μg/mL). **(b)** Heating profile of MoS$_2$-IO-(d)PEG solutions with different concentrations under exposure to an 808 nm laser for 5 min at a power density of 0.7 W cm^{-2}. **(c)** Magnetization hysteresis loops of MoS$_2$-IO and MoS$_2$-IO-(d)PEG. Inset is the enlargement at the (0, 0) region. The decrease of magnetization value (emu/g) of the material after PEGylation was attributed to the added PEG weight. **(d)** T2-weighted MR images and T2 relaxation rates (r_2) of MoS$_2$-IO-(d)PEG measured at various Fe concentrations.

not demonstrated in this work, the free amine groups on the surface of MoS$_2$-IO-(d)PEG sheets would be available for conjugation of other functional biomolecules (*e.g.*, fluorescent dyes, targeting molecules). The final nanocomposites showed neutralized surface charge (Supporting Figure S2a), which is also preferred for applications in biological environments.[35] Notably, direct conjugation of amine-terminated branched PEG to as-made MoS$_2$-IO was not as effective owing to the salt-induced aggregation of nanomaterials during the conjugation process, in which 1-ethyl-3-(3-(dimethylamino)propyl)carbodiimide·HCl (EDC·HCl) was added to trigger the amide formation.

The optical properties of the obtained MoS$_2$-IO-(d)PEG were then studied. Decoration of IONPs, which absorb strongly at the short-wavelength range, did not significantly alter the NIR absorbance of MoS$_2$ nanosheets. Single or double PEG modification to the surface of MoS$_2$-IO nanocomposites showed no obvious effects on the UV−vis−NIR extinction spectra of our nanocomposites (Figure 2a). Thus, the decoration of IONPs and double PEGylation, although changing the surface structures of MoS$_2$ nanosheets by chemical reaction, did not lessen their absorbance in the NIR tissue-transparent window. The photothermal conversion ability of MoS$_2$-IO-(d)PEG was then tested by monitoring the multiple portion dilutions of MoS$_2$-IO-(d)PEG, which were irradiated with a 808 nm laser at a relative low power density (0.7 W cm^{-2}) *via* an IR thermal camera. The heating curves of these solutions, similar to MoS$_2$ nanosheets,[17] showed rapid heating and large

temperature increment depending on the concentrations (Figure 2b). The photothermal conversion efficiency of MoS$_2$-IO-(d)PEG remained unchanged even after five rounds of heating and cooling, revealing its robust photothermal stability (Supporting Figure S4b).

Ultrasmall superparamagnetic IONPs have been extensively used as the contrast agent in MR imaging.[36] The magnetic property of MoS$_2$-IO-(d)PEG was then studied by the field-dependent magnetization measurement. As evidenced by the hysteresis loops in their magnetization curves (Figure 2c), both MoS$_2$-IO and MoS$_2$-IO-(d)PEG appeared to have the superparamagnetic feature. T2-weighted MR imaging of MoS$_2$-IO-(d)PEG samples by a 3-T MR scanner revealed a concentration-dependent darkening effect, with the transverse relaxivity coefficient (r2) calculated to be 93.59 mM^{-1} s^{-1} (Figure 2d), demonstrating the capability of MoS$_2$-IO-(d)PEG to offer T2 contrast in MR imaging.

Before moving on toward further *in vivo* studies, the intrinsic toxicity of MoS$_2$-IO nanosheets before and after S/D PEGylation was tested *in vitro*. 4T1 murine breast cancer cells and RAW 264.7 mouse macrophage cells were respectively cultured with MoS$_2$-IO, MoS$_2$-IO-(s) PEG, and MoS$_2$-IO-(d) PEG at various concentrations for 24 h. While MoS$_2$-IO- and MoS$_2$-IO-(s)PEG-incubated cells showed obviously reduced viabilities under relatively high MoS$_2$ concentrations, MoS$_2$-IO-(d)PEG, with a more stable PEG coating, exhibited remarkably reduced toxicity to both types of cell lines (Supporting Figure S5).
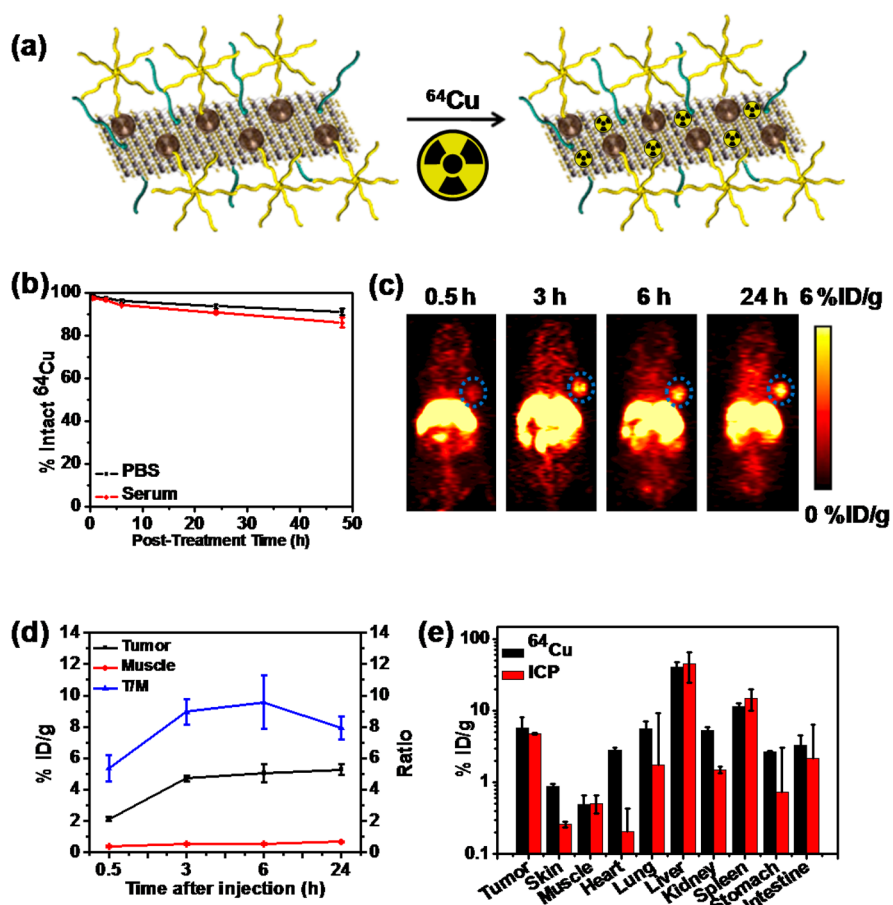
Figure 3. ^{64}Cu labeling on MoS$_2$-IO-(d)PEG for PET imaging. (a) Scheme presenting the ^{64}Cu labeling on MoS$_2$-IO-(d)PEG *via* a chelator-free manner. (b) Stability test of ^{64}Cu labeling on MoS$_2$-IO-(d)PEG after incubation in PBS and serum for different periods of time. (c) PET images of 4T1 tumor-bearing mice taken at various time points post iv injection of ^{64}Cu-MoS$_2$-IO-(d)PEG. The blue dot circles highlight the 4T1 tumor site of mice. (d) Quantification of ^{64}Cu-MoS$_2$-IO-(d)PEG uptake in the tumor and muscle, as well as the tumor/muscle (T/M) ratio at various time points pi. (e) Biodistribution of MoS$_2$-IO-(d)PEG 24 h after iv injection into 4T1 tumor-bearing mice as determined by either ^{64}Cu radioactivity measurement or ICP-AES-measured Mo concentrations in various organs and tissues. Error bars were based on the standard error of the mean (SEM) of quadruplicate samples. The unit is the percentage of injected dose per gram of tissue (%ID/g).

To further verify the superiority of double PEGylation, both MoS$_2$-IO-(d)PEG and MoS$_2$-IO-(s)PEG nanosheets ([MoS$_2$] = 0.68 mg mL^{-1}, 0.2 mL) were intravenously (iv) injected into mice. The blood circulation behaviors of our nanocomposites with either single or double PEGylation were studied by ICP-AES measurement of Mo^{2+} levels in blood samples collected at various time points postinjection (Supporting Figure S6). Compared to MoS$_2$-IO-(s)PEG, MoS$_2$-IO-(d)PEG exhibited remarkably prolonged retention in the blood after iv injection. It was likely because the condensed PEG coating on the surface was able to delay the macrophage clearance of those nanoparticles in reticuloendothelial systems (RES).[37,38] Therefore, it is clear that double PEGylation could offer our nanocomposites obviously enhanced biocompability and more favorable pharmacokinetics. MoS$_2$-IO-(d)PEG was thus chosen in our following *in vivo* experiments.

PET imaging, which has excellent sensitivity and superb tissue penetration of signal, has been widely adopted in clinical patient management (diagnosis,

staging, treatment monitoring, *etc.*).[39] However, to label biomolecules or nanoparticles with radiometal ions such as ^{64}Cu, conjugation with chelator molecules such as 1,4,7-triazacyclononane-1,4,7-triacetic acid (NOTA) or 1,4,7,10-tetraazacyclododecane-1,4,7,10-tetraacetic acid (DOTA) is usually a required procedure.[40,41] Chelator-free radiolabeling has recently emerged as a promising alternative approach to label nanoparticles in a facile way without changing their surface coating chemistry as well as native pharmacokinetic profiles[42,43] and in the mean time leaving their functional groups intact for further modification or bioconjugation. Considering the high affinity between Cu^{2+} ions and sulfur atoms,[43] we thus hypothesized that our MoS$_2$-IO-(d)PEG could be labeled in a chelator-free manner. In this study, ^{64}Cu labeling was straightforwardly executed by mixing ^{64}CuCl$_2$ with MoS$_2$-PEG or MoS$_2$-IO-(d)PEG at 37 °C for 60 min under constant shaking (Figure 3a). As determined by thin-layer chromatography (TLC) (Supporting Figure S7a) at different points of time, we found that ^{64}Cu was immediately
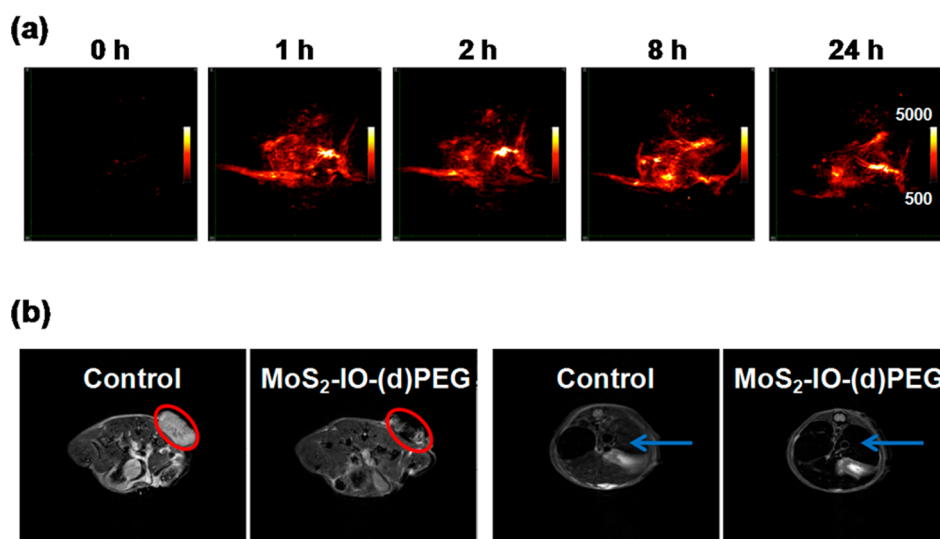
Figure 4. *In vivo* PAT and MR imaging. (a) PAT images of 4T1 tumor on mice acquired before and at various time points after iv injection with MoS$_2$-IO-(d)PEG (dose of MoS$_2$ = 6.85 mg/kg). (b) T2-weighted MR images showing the transverse sections of a tumor-bearing mouse before and after injection with MoS$_2$-IO-(d)PEG (dose of MoS$_2$ = 6.85 mg/kg). The red circles and blue arrows highlight the 4T1 tumor and liver of mice, respectively.

adsorbed onto MoS$_2$-PEG and MoS$_2$-IO-(d)PEG nanosheets, with labeling yields measured to be as high as 85% and 70% after 60 min of incubation, respectively (Supporting Figure S7b). In contrast, the control experiment by labeling PEGylated IONPs with ^{64}Cu by the same procedure resulted in a negligible labeling yield, suggesting that free ^{64}Cu ions could be attached on the surface of MoS$_2$ nanosheets but not on IONPs. Such labeling is possibly due to the anchoring of Cu^{2+} ions on the Mo defect sites of MoS$_2$ nanosheets.

To ensure that the ^{64}Cu labeling on MoS$_2$-IO-(d)PEG was sufficiently stable for *in vivo* applications, a serum stability test was carried out. After incubation in PBS and serum at 37 °C for different periods of time, ^{64}Cu-MoS$_2$-IO-(d)PEG solutions were washed through 100 kDa filters to remove detached ^{64}Cu. By measuring the remaining radioactivities in those samples, we found that ^{64}Cu labeling in ^{64}Cu-MoS$_2$-IO-(d)PEG was highly stable within 48 h in serum (Figure 3b). Therefore, ^{64}Cu-labeled MoS$_2$-IO-(d)PEG could be adopted as a noninvasive PET imaging contrast agent to precisely reveal its biodistribution and pharmacokinetics *in vivo*.

Encouraged by the feasibility and physiological stability of ^{64}Cu labeling on our nanoagent, PET scans of 4T1 tumor-bearing mice at various time points post intravenous (iv) injection of ^{64}Cu-MoS$_2$-IO-(d)PEG (5−10 MBq) were performed using a microPET Inveon rodent model scanner (Figure 3c). Obvious tumor contrast was observed at 3 h after injection, suggesting effective tumor retention of nanocomposites due to the enhanced permeability and retention effect (EPR) of cancerous tumors.[44,45] Quantitative PET data presented as percentage injected dose per gram of tissue (%ID/g) further confirmed the time-dependent increase of ^{64}Cu signals in the tumor postinjection of ^{64}Cu-MoS$_2$-IO-(d)PEG (Figure 3d). In order to further understand the *in vivo* biodistribution of MoS$_2$-IO-(d)PEG, mice were sacrificed 24 h after injection of ^{64}Cu-labeled nanocomposites, and the radioactivities in major tissues and organs were measured using a γ-counter (Figure 3e). In addition to the tumors, high radioactivities were also noted in liver and spleen, which were RES organs responsible for the clearance of foreign nanoparticles by macrophage uptake.[46] Notably, the *ex vivo* biodistribution data acquired based on ^{64}Cu matched reasonably well with that obtained by ICP-AES measurement of Mo levels in tissue lysates, indicating that ^{64}Cu labeling on MoS$_2$-IO-(d)PEG was rather stable *in vivo*.

Photoacoustic tomography imaging is a newly developed method combining the high contrast of optical imaging and deep tissue penetration of ultrasound based on the photoacoustic effect.[47] In PAT imaging, optical energy absorbed by light-absorbing tissues or contrasting agents results in thermoelastic expansion that creates reflected ultrasound signals.[48] In our experiments, mice were iv injected with MoS$_2$-IO-(d)PEG nanosheets ([MoS$_2$] = 0.68 mg mL^{-1}, 0.2 mL). Compared to the PAT image of tumor before injection, strong PAT signals were detected after iv injection of MoS$_2$-IO-(d)PEG (Figure 4a), suggesting highly efficient tumor retention of our NIR-absorbing nanoagent.

While PET imaging confers high sensitivity and quantitative tracking of positron-emitting radiotracers and PAT imaging provides useful information regarding the distribution of nanoparticles inside the tumor, MR imaging would be able to show high soft-tissue contrast with anatomic information.[22] For MR imaging, 4T1 tumor-bearing mice iv injected with MoS$_2$-IO-(d)PEG were imaged in a 9 T MR scanner before
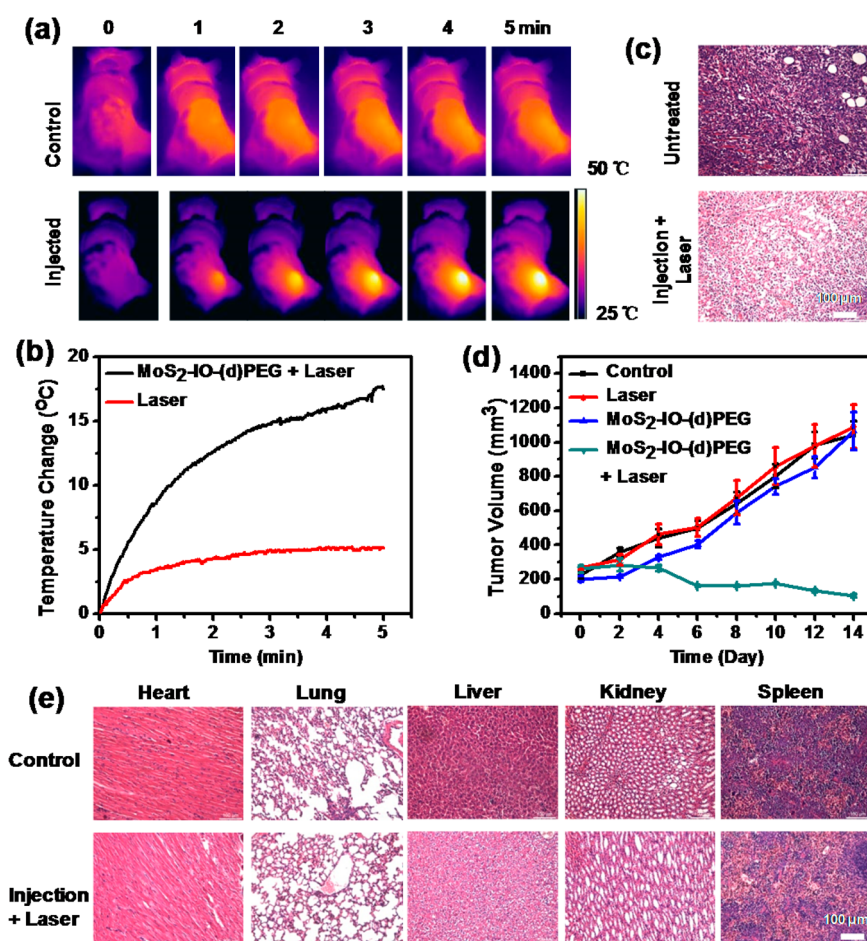
Figure 5. *In vivo* photothermal therapy. (a) IR thermal images of 4T1 tumor-bearing mice without or with iv injection of MoS$_2$-IO-(d)PEG (dose of MoS$_2$ = 6.85 mg/kg) under 808 nm laser irradiation (0.78 W cm^{-2}) taken at different time intervals. The irradiation was conducted 8 h after injection. (b) Average temperature change at the tumor site of mice during laser irradiation as indicated in (a). (c) H&E stained images of tumors sliced from an untreated mouse (upper) and a mouse 1 day after MoS$_2$-IO-(d)PEG-induced photothermal treatment. (d) Tumor volume growth on mice (5 mice for each group) measured after various treatments indicated every 2 days for 2 weeks. (e) H&E stained images of major organs of healthy mice and mice 14 days post MoS$_2$-IO-(d)PEG injection and photothermal treatment.

injection and at 24 h postinjection (pi) ([MoS$_2$] = 0.68 mg mL^{-1}, optical density (OD) = 20, 0.2 mL). Compared to untreated mice, the tumor of mice 24 h pi showed obvious darkening effects in T2-weighted MR images, indicating the prominent passive accumulation of MoS$_2$-IO-(d)PEG in the tumor (Figure 4b). Meanwhile, RES organs such as the liver also showed strong darkening contrast (Supporting Figure S8), consistent with PET imaging results.

In vivo PAT/MR/PET trimodal imaging vividly showed the effective, time-dependent tumor retention of MoS$_2$-IO-(d)PEG upon systemic administration. Utilizing the strong NIR absorbance attributed to MoS$_2$, *in vivo* photothermal therapy with MoS$_2$-IO-(d)PEG was then conducted in the animal tumor model. Female Balb/c mice bearing 4T1 murine breast cancer tumors were randomly divided into four groups with 5 mice per group. Under the guidance of imaging, which revealed that the tumor accumulation of MoS$_2$-IO-(d)PEG reached a high level at ~8 h postinjection, each mouse in the treatment group was exposed to an

808 nm laser (0.78 W cm^{-2}, 5 min) 8 h after iv injection of MoS$_2$-IO-(d)PEG ([MoS$_2$] = 0.68 mg mL^{-1}, 20 OD, 0.2 mL). The three groups include untreated mice, mice treated only with nanomaterials injection (no laser), and mice treated only with laser irradiation (no nanomaterials injection) as controls. As monitored by an IR thermal camera during irradiation, the surface temperature of tumors quickly increased to ~51 °C for nanomaterials-injected mice within 5 min, a temperature sufficient for tumor eradiation (Figure 5a). In remarkable contrast, the temperatures of tumors in mice without injection gently increased by only ~5 °C under laser exposure (Figure 5b). As revealed by micrographs of a hematoxylin and eosin (H&E) stained tumor slice, prominent cell damage was found in the tumor after MoS$_2$-IO-(d)PEG-induced photothermal ablation (Figure 5c). Tumor sizes of mice in each group were then measured every 2 days after various treatments over 2 weeks (Figure 5d). While laser irradiation alone showed no influence on tumor growth, injection of MoS$_2$-IO-(d)PEG alone also offered no significant

effect to restrain the tumor development. In contrast, tumors on mice injected with MoS$_2$-IO-(d)PEG and then exposed to NIR laser triggered photothermal therapy were completely eliminated (Supporting Figure S9). Our results suggest that MoS$_2$-IO-(d)PEG is a powerful agent for *in vivo* photothermal therapy of cancer.

Lastly, we examined the potential toxic side effects of MoS$_2$-IO-(d)PEG to treated mice. No obvious body weight loss (Supporting Figure S10) or abnormal behavior was seen for MoS$_2$-IO-(d)PEG-injected mice during our experiments. Mice iv injected with MoS$_2$-IO-(d)PEG were sacrificed 14 days after PTT treatment, with major organs collected and sliced for histology analysis (Figure 5e). No appreciable organ damage or inflammatory lesion was detected in all major organs of mice, preliminarily proving that MoS$_2$-IO-(d)PEG was not noticeably toxic at the tested dose to animals.

CONCLUSION

In summary, a novel 2D nanocomposite by self-assembly of IONPs on MoS$_2$ nanosheets is successfully fabricated and functionalized with dual PEG coatings to achieve enhanced biocompatibility. Such a nanocomposite could be efficiently labeled with PET isotope ^{64}Cu by simple mixing without the need of chelation chemistry. In this system, DMSA-functionalized IONPs and lipoic acid-modified PEG both with thiol groups are anchored to the S defects on MoS$_2$ nanosheets. Amine-terminated PEG is then conjugated to the carboxyl groups on the IONP surface to offer further improved surface coating by double PEGylation. Afterward, ^{64}Cu ions could be stably adsorbed on the surface of MoS$_2$ likely *via* doping into the Mo defects (by Cu—S bonding) to enable nuclear imaging. Utilizing ^{64}Cu-labeled MoS$_2$-IO-(d)PEG, which in the meantime exhibits high NIR absorbance and strong T2MR contrast, triple modal PET, PAT, and MR imaging has been conducted on 4T1 tumor-bearing mice, revealing time-dependent tumor retention of nanoparticles after iv injection. Photothermal therapy is then carried out on MoS$_2$-IO-(d)PEG-injected mice, resulting in complete elimination of 4T1 murine breast tumors on treated mice. Our work shows the great potential of TMDCs as a 2D platform to construct nanoscale theranostic agents with highly integrated functionalities. Moreover, the novel chemistry approaches on MoS$_2$ nanosheets presented in this work may contribute to the development of metal sulfide-based nanocomposites for a wide range of applications, not only in biomedicine but also in other fields.

EXPERIMENTAL SECTION

1. Synthesis of DMSA-IONPs. All chemicals, unless specified otherwise, were purchased from Sigma-Aldrich and used as received. Iron oxide nanoparticles were synthesized in a typical organic-phase synthesis procedure.[49] Briefly, Fe(acac)$_3$ (2 mmol), 1,2-dodecanediol (10 mmol), oleic acid (6 mmol), oleylamine (6 mmol), and benzyl ether (20 mL) were added into a three-necked flask. After magnetically stirring under a flow of nitrogen, the mixture was heated to 200 °C for 2 h and then heated to 300 °C for 1 h. Nitrogen protection was maintained in the whole course. After cooling to room temperature, the black-colored mixture was precipitated by ethanol (40 mL) under ambient conditions. The sediment was washed by hexane and ethanol several times and redispersed into tetrahydrofuran (THF) at the concentration of 5 mg mL^{-1}.

To functionalize IONPs, 100 mg of DMSA was dissolved in 1 mL of deionized water at pH ~10 and then dropwisely added into 20 mg of IONPs dispersed in 4 mL of THF under sonication. After further sonication for 1 h and then stirring for 3 h, this solution was washed with water by centrifugation at 14 800 rpm for 5 min to remove THF and excess DMSA. The precipitated DMSA-modified IONPs were finally dispersed in 4 mL of deionized water for further use.

2. Synthesis of MoS$_2$-IO-(d)PEG. MoS$_2$ nanosheets were synthesized by the Morrison method. Typically, 5 mL of *n*-butyllithium in hexane was added to dissolve 1 mg of MoS$_2$ bulk powder in a glovebox under the protection of nitrogen gas. After 2 days of intercalation, the MoS$_2$ solution was washed by hexane. The precipitate was taken out from the glovebox and then dissolved into 100 mL of deionized water. During ultrasonication, the lithium atoms between MoS$_2$ layers reacted with water and rapidly produced copious hydrogen gas to push MoS$_2$ nanosheets away from each other. Lastly, multilayered MoS$_2$ was discarded by centrifugation under 6000 rpm for 15 min, and excess hexane and lithium ions were removed by dialyzing against deionized water, yielding water-soluble single-layered MoS$_2$ nanosheets.

To prepare MoS$_2$-IO nanocomposites, an aqueous solution of MoS$_2$ nanosheets (1 mg mL^{-1}) was slowly added into an aqueous solution of DMSA-modified IONPs (1 mg mL^{-1}) at different feeding mass ratios (MoS$_2$:IONPs = 1:2, 1:5, and 1:10) under sonication. After magnetic stirring overnight, the nanocomposites were precipitated by adding saline and centrifugation. The obtained MoS$_2$-IONPs were redispersed in water with a concentration of 1 mg mL^{-1}.

Lipoic acid terminated polyethylene glycol (LA-PEG) was synthesized following a reported protocol.[50] A 10 mg amount of LA-PEG was added into 12 mg of MoS$_2$-IO (2 mg of MoS$_2$) in water under sonication. The solution was then stirred overnight to modify MoS$_2$ nanosheets *via* sulfur chemistry, obtaining MoS$_2$-IO-(s)PEG with better stability in PBS. For further PEGylation, 10 mg of 6-arm-PEG-amine (10 kDa) was mixed with MoS$_2$-IO-(s) PEG. Then 10 mg of EDC was added every 30 min three times to initiate the reaction between amino groups on the 6-arm-PEG-amine and the carboxyl group on DMSA-modified IONPs. Excess PEG polymers were removed by centrifugal filtration with 100 kDa molecular weight cutoff (MWCO) filters (Millipore) and several water washings. The obtained MoS$_2$-IO-(d)PEG was redispersed in water for further use.

3. Characterization. TEM images were obtained using a FEI Tecnai F20 transmission electron microscope at an acceleration voltage of 200 kV. UV—vis—NIR spectra were obtained with a PerkinElmer Lambda 750 UV—vis—NIR spectrophotometer. Heating curves were recorded by an IR thermal camera (IRS E50 Pro thermal imaging camera). The real ratios of MoS$_2$ and IONPs were tested by ICP-AES (Vista Mpx 700-ES).

4. Cell Culture and MTT Assay. All cell-culture-related reagents were purchased from Hyclone. 4T1 cells (a murine breast cancer cell line) and RAW 264.7 (a mouse macrophage cell line) were cultured in RPMI-1640 medium supplemented with 10% fetal bovine serum (FBS) and 1% penicillin/streptomycin. For the *in vitro* cell toxicity test, 4T1 cells were seeded on 96-well plates and then incubated with MoS$_2$-IO, MoS$_2$-IO-(s)PEG, or MoS$_2$-IO-(d)PEG for 24 h. The standard cell viability assay using 3-(4,5-dimethylthiazol-2-yl)-2,5-diphenyltetrazolium bromide (MTT)

was carried out to determine cell viabilities relative to control cells incubated with the same volume of PBS.

5. ^{64}Cu-Labeling and Serum Stability Studies. Complete mouse serum was purchased from Jackson Immuno Research Laboratories (West Grove, PA, USA). MWCO Amicon filters were purchased from Millipore (Billerica, MA, USA). PD-10 desalting columns were purchased from GE Healthcare (Piscataway, NJ, USA). Chelex 100 resin (50−100 mesh) was purchased from Sigma-Aldrich (St. Louis, MO, USA). Water and all buffers were of Millipore grade and pretreated with Chelex 100 resin to ensure that the aqueous solution was free of heavy metal ions. All the other reaction buffers and chemicals were obtained from Thermo Fisher Scientific (Fair Lawn, NJ, USA).

^{64}Cu was produced with an onsite cyclotron (GE PETtrace). ^{64}CuCl$_2$ (148 MBq) was diluted in 300 mL of 0.1 M sodium acetate buffer (pH 5.5) and mixed with 30 μL of MoS$_2$-IO-(d)PEG (2 mg mL^{-1}). The reaction was conducted at 37 °C for 60 min with constant shaking, and the labeling yield was determined by TLC at different time points. The resulting ^{64}Cu- MoS$_2$-IO-(d)PEG was purified by a PD-10 column using PBS as the mobile phase.

To ensure that ^{64}Cu-MoS$_2$-IO-(d)PEG was sufficiently stable for *in vivo* applications, serum stability studies were carried out. ^{64}Cu-MoS$_2$-IO-(d)PEG was incubated in complete mouse serum and PBS at 37 °C for up to 48 h. Portions of the mixture were sampled at different time points and filtered through 100 kDa MWCO filters. The radioactivity that remained on the filter was measured after discarding the filtrate, and retained (*i.e.*, intact) ^{64}Cu-MoS$_2$-IO-(d)PEG was calculated using the equation (radioactivity on filter/total radioactivity) × 100%.

6. Animal Model for PET Imaging. 4T1 murine breast cancer cells were used for 4T1 tumor implantation when they reached ∼80% confluence. All animal studies for PET imaging were conducted under a protocol approved by the University of Wisconsin Institutional Animal Care and Use Committee. Four- to five-week-old female BALB/c mice (Harlan, Indianapolis, IN, USA) were each injected with 2 × 10^6 4T1 cells in the flank to generate the 4T1 breast cancer model. The mice were used for *in vivo* experiments when the tumor diameter reached 6−8 mm.

PET scans of 4T1 tumor-bearing mice (4 mice per group) at various time points post iv injection of 5−10 MBq of ^{64}Cu-MoS$_2$-IO-(d)PEG were performed using a microPET/microCT Inveon rodent model scanner (Siemens Medical Solutions USA, Inc.). Data acquisition, image reconstruction, and region-of-interest analysis of the PET data were performed as described previously.[51−54] Quantitative PET data of the 4T1 tumor and major organs were presented as percentage injected dose per gram of tissue (%ID/g). After the last scan at 24 h pi, biodistribution studies were carried out to confirm that the %ID/g values based on PET imaging truly represented the radioactivity distribution in mice. Mice were euthanized, and 4T1 tumor, blood, and major organs/tissues were collected and wet-weighed. The radioactivity in the tissue was measured using a γ-counter (PerkinElmer) and presented as %ID/g (mean ± SD).

7. In Vivo PAT and MR Imaging. Balb/c mice bearing 4T1 tumors were intravenously injected with MoS$_2$-IO-(d)PEG ([MoS$_2$] = 6.85 mg/kg, 20 OD, 0.2 mL) before imaging. PAT imaging was conducted by a photoacoustic computed tomography scanner (Endra Nexus 128, Ann Arbor, MI, USA). During PAT imaging, anesthesia was maintained using pentobarbital (50 mg/kg) and the body temperature of the mice was kept constant by a water heating system at 37.5 °C. T2-weighted MR imaging was performed by a 9.4T MR scanner designed for small animal imaging (Bruker Biospin Corporation, Billerica, MA, USA).

8. In Vivo Photothermal Therapy. All animal experiments for photothermal therapy were carried out under protocols approved by Soochow University Laboratory Animal Center. To develop the tumor model, 4T1 cells (1 × 10^6) suspended in 40 μL of PBS were subcutaneously injected into the back of each Balb/c mouse. After the tumor volume reached ∼50 mm^3, mice were randomly divided into four groups (*n* = 5 per group): untreated, laser only, MoS$_2$-IO-(d)PEG only, and laser irradiation postinjection of MoS$_2$-IO-(d)PEG. The dose of MoS$_2$ in MoS$_2$-IO-(d)PEG was 6.85 mg/kg (20 OD, 0.2 mL). Laser irradiation was

conducted 8 h after injection of MoS$_2$-IO-(d)PEG by the 808 nm laser for 5 min at 0.78 W cm^{-2} for photothermal treatment. The tumor sizes were measured after treatments by a digital caliper every 2 days for 2 weeks. The tumor volume was calculated according to the following formula: width^2 × length/2. Error bars are based on standard errors of the mean.

9. Histology Analysis. Three female Balb/c control mice were respectively sacrificed 1, 2, and 14 days after iv injection of MoS$_2$-IO-(d)PEG ([MoS$_2$] = 6.85 mg/kg) and treatment of PTT. Tumor and major organs including heart, kidney, liver, lung, and spleen from those mice were harvested and fixed in 4% formaldehyde solution. Later, these tumors and organs were processed routinely into paraffin, sectioned at 8 μm thickness, stained with H&E, and examined with a digital microscope (Leica QWin).

Conflict of Interest: The authors declare no competing financial interest.

Supporting Information Available: Supporting Figures S1−10. This material is available free of charge *via* the Internet at http://pubs.acs.org.

REFERENCES AND NOTES

1. Novoselov, K.; Jiang, D.; Schedin, F.; Booth, T.; Khotkevich, V.; Morozov, S.; Geim, A. Two-Dimensional Atomic Crystals. *Proc. Natl. Acad. Sci. U.S.A.* **2005**, *102*, 10451–10453.

2. Butler, S. Z.; Hollen, S. M.; Cao, L.; Cui, Y.; Gupta, J. A.; Gutiérrez, H. R.; Heinz, T. F.; Hong, S. S.; Huang, J.; Ismach, A. F. Progress, Challenges, and Opportunities in Two-Dimensional Materials beyond Graphene. *ACS Nano* **2013**, *7*, 2898–2926.

3. Huang, X.; Zeng, Z.; Zhang, H. Metal Dichalcogenide Nanosheets: Preparation, Properties and Applications. *Chem. Soc. Rev.* **2013**, *42*, 1934–1946.

4. Chen, Y.; Tan, C.; Zhang, H.; Wang, L. Two-Dimensional Graphene Analogues for Biomedical Applications. *Chem. Soc. Rev.* **2015**, 10.1039/C4CS00300D.

5. Wang, Q. H.; Kalantar-Zadeh, K.; Kis, A.; Coleman, J. N.; Strano, M. S. Electronics and Optoelectronics of Two-Dimensional Transition Metal Dichalcogenides. *Nat. Nanotechnol.* **2012**, *7*, 699–712.

6. Peng, H.; Dang, W.; Cao, J.; Chen, Y.; Wu, D.; Zheng, W.; Li, H.; Shen, Z.-X.; Liu, Z. Topological Insulator Nanostructures for Near-Infrared Transparent Flexible Electrodes. *Nat. Chem.* **2012**, *4*, 281–286.

7. Yin, Z.; Li, H.; Li, H.; Jiang, L.; Shi, Y.; Sun, Y.; Lu, G.; Zhang, Q.; Chen, X.; Zhang, H. Single-Layer MoS$_2$ Phototransistors. *ACS Nano* **2011**, *6*, 74–80.

8. Soon, J. M.; Loh, K. P. Electrochemical Double-Layer Capacitance of MoS$_2$ Nanowall Films. *Electrochem. Solid State* **2007**, *10*, A250–A254.

9. Du, G.; Guo, Z.; Wang, S.; Zeng, R.; Chen, Z.; Liu, H. Superior Stability and High Capacity of Restacked Molybdenum Disulfide as Anode Material for Lithium Ion Batteries. *Chem. Commun.* **2010**, *46*, 1106–1108.

10. Chhowalla, M.; Shin, H. S.; Eda, G.; Li, L.-J.; Loh, K. P.; Zhang, H. The Chemistry of Two-Dimensional Layered Transition Metal Dichalcogenide Nanosheets. *Nat. Chem.* **2013**, *5*, 263–275.

11. Chianelli, R. R.; Siadati, M. H.; De La Rosa, M. P.; Berhault, G.; Wilcoxon, J. P.; Bearden, R., Jr.; Abrams, B. L. Catalytic

Properties of Single Layers of Transition Metal Sulfide Catalytic Materials. *Catal. Rev.* **2006**, *48*, 1–41.

12. Chou, S. S.; De, M.; Kim, J.; Byun, S.; Dykstra, C.; Yu, J.; Huang, J.; Dravid, V. P. Ligand Conjugation of Chemically Exfoliated MoS₂. *J. Am. Chem. Soc.* **2013**, *135*, 4584–4587.

13. Chou, S. S.; Kaehr, B.; Kim, J.; Foley, B. M.; De, M.; Hopkins, P. E.; Huang, J.; Brinker, C. J.; Dravid, V. P. Chemically Exfoliated MoS₂ as Near-Infrared Photothermal Agents. *Angew. Chem.* **2013**, *125*, 4254–4258.

14. Cheng, L.; Liu, J.; Gu, X.; Gong, H.; Shi, X.; Liu, T.; Wang, C.; Wang, X.; Liu, G.; Xing, H. Imaging: PEGylated WS2 Nanosheets as a Multifunctional Theranostic Agent for in Vivo Dual-Modal CT/Photoacoustic Imaging Guided Photothermal Therapy. *Adv. Mater.* **2014**, *26*, 1794–1794.

15. Li, J.; Jiang, F.; Yang, B.; Song, X.-R.; Liu, Y.; Yang, H.-H.; Cao, D.-R.; Shi, W.-R.; Chen, G.-N. Topological Insulator Bismuth Selenide as a Theranostic Platform for Simultaneous Cancer Imaging and Therapy. *Sci. Rep.* **2013**, *3*, 1998.

16. Zhu, C.; Zeng, Z.; Li, H.; Li, F.; Fan, C.; Zhang, H. Single-Layer MoS₂-Based Nanoprobes for Homogeneous Detection of Biomolecules. *J. Am. Chem. Soc.* **2013**, *135*, 5998–6001.

17. Liu, T.; Wang, C.; Gu, X.; Gong, H.; Cheng, L.; Shi, X.; Feng, L.; Sun, B.; Liu, Z. Drug Delivery with PEGylated MoS₂ Nano-Sheets for Combined Photothermal and Chemotherapy of Cancer. *Adv. Mater.* **2014**, *26*, 3433–3440.

18. Liu, T.; Wang, C.; Cui, W.; Gong, H.; Liang, C.; Shi, X.; Li, Z.; Sun, B.; Liu, Z. Combined Photothermal and Photodynamic Therapy Delivered by PEGylated MoS₂ Nanosheets. *Nanoscale* **2014**, *6*, 11219–11225.

19. Chen, Q.; Liang, C.; Wang, X.; He, J.; Li, Y.; Liu, Z. An Albumin-Based Theranostic Nano-Agent for Dual-Modal Imaging Guided Photothermal Therapy to Inhibit Lymphatic Metastasis of Cancer Post Surgery. *Biomaterials* **2014**, *35*, 9355–9362.

20. Gong, H.; Dong, Z.; Liu, Y.; Yin, S.; Cheng, L.; Xi, W.; Xiang, J.; Liu, K.; Li, Y.; Liu, Z. Engineering of Multifunctional Nano-Micelles for Combined Photothermal and Photodynamic Therapy under the Guidance of Multimodal Imaging. *Adv. Funct. Mater.* **2014**, *24*, 6492–6502.

21. Ma, X.; Tao, H.; Yang, K.; Feng, L.; Cheng, L.; Shi, X.; Li, Y.; Guo, L.; Liu, Z. A Functionalized Graphene Oxide-Iron Oxide Nanocomposite for Magnetically Targeted Drug Delivery, Photothermal Therapy, and Magnetic Resonance Imaging. *Nano Res.* **2012**, *5*, 199–212.

22. Judenhofer, M. S.; Wehrl, H. F.; Newport, D. F.; Catana, C.; Siegel, S. B.; Becker, M.; Thielscher, A.; Kneilling, M.; Lichy, M. P.; Eichner, M. Simultaneous PET-MRI: A New Approach for Functional and Morphological Imaging. *Nat. Med.* **2008**, *14*, 459–465.

23. Kim, J.; Piao, Y.; Hyeon, T. Multifunctional Nanostructured Materials for Multimodal Imaging, and Simultaneous Imaging and Therapy. *Chem. Soc. Rev.* **2009**, *38*, 372–390.

24. Qin, C.; Cheng, K.; Chen, K.; Hu, X.; Liu, Y.; Lan, X.; Zhang, Y.; Liu, H.; Xu, Y.; Bu, L. Tyrosinase as a Multifunctional Reporter Gene for Photoacoustic/MRI/PET Triple Modality Molecular Imaging. *Sci. Rep.* **2013**, *3*, 1490.

25. Chen, H.; Wang, G. D.; Tang, W.; Todd, T.; Zhen, Z.; Tsang, C.; Hekmatyar, K.; Cowger, T.; Hubbard, R. B.; Zhang, W. Gd-Encapsulated Carbonaceous Dots with Efficient Renal Clearance for Magnetic Resonance Imaging. *Adv. Mater.* **2014**, *26*, 6761–6766.

26. Zhang, Y.; Jeon, M.; Rich, L. J.; Hong, H.; Geng, J.; Zhang, Y.; Shi, S.; Barnhart, T. E.; Alexandridis, P.; Huizinga, J. D. Non-Invasive Multimodal Functional Imaging of the Intestine with Frozen Micellar Naphthalocyanines. *Nat. Nanotechnol.* **2014**, *9*, 631–638.

27. Sumer, B.; Gao, J. Theranostic Nanomedicine for Cancer. *Future Med.* **2008**, *3*, 137–140.

28. Liu, Y.; Yin, J.-J.; Nie, Z. Harnessing The Collective Properties of Nanoparticle Ensembles for Cancer Theranostics. *Nano Res.* **2014**, 1–12.

29. Xie, J.; Lee, S.; Chen, X. Nanoparticle-Based Theranostic Agents. *Adv. Drug Delivery Rev.* **2010**, *62*, 1064–1079.

30. Milosevic, I.; Motte, L.; Saboungi, M.-L.; Aoun, B.; Li, T.; Sun, C.; Ren, Y. Superparamagnetic Nanoplatforms for

31. Coleman, J. N.; Lotya, M.; O'Neill, A.; Bergin, S. D.; King, P. J.; Khan, U.; Young, K.; Gaucher, A.; De, S.; Smith, R. J. Two-Dimensional Nanosheets Produced by Liquid Exfoliation of Layered Materials. *Science* **2011**, *331*, 568–571.

32. Hassel, O. Ueber Die Kristallstruktur Des Molybdaenglanzes. *Z. Kristallogr., Kristallgeom., Kristallphys., Kristallchem.* **1925**, *61*, 92–99.

33. Huang, X.; Zeng, Z.; Bao, S.; Wang, M.; Qi, X.; Fan, Z.; Zhang, H. Solution-Phase Epitaxial Growth of Noble Metal Nanostructures on Dispersible Single-Layer Molybdenum Disulfide Nanosheets. *Nat. Commun.* **2013**, *4*, 1444.

34. Chen, Y.; Song, B.; Tang, X.; Lu, L.; Xue, J. Ultrasmall Fe₃O₄ Nanoparticle/MoS₂ Nanosheet Composites with Superior Performances for Lithium Ion Batteries. *Small* **2014**, *10*, 1536–1543.

35. Choi, H. S.; Liu, W.; Misra, P.; Tanaka, E.; Zimmer, J. P.; Ipe, B. I.; Bawendi, M. G.; Frangioni, J. V. Renal Clearance of Quantum Dots. *Nat. Biotechnol.* **2007**, *25*, 1165–1170.

36. Jun, Y. W.; Lee, J. H.; Cheon, J. Chemical Design of Nanoparticle Probes for High-Performance Magnetic Resonance Imaging. *Angew. Chem.* **2008**, *47*, 5122–5135.

37. Moghimi, S.; Szebeni, J. Stealth Liposomes and Long Circulating Nanoparticles: Critical Issues in Pharmacokinetics, Opsonization and Protein-Binding Properties. *Prog. Lipid Res.* **2003**, *42*, 463–478.

38. Cheng, L.; Yang, K.; Chen, Q.; Liu, Z. Organic Stealth Nanoparticles for Highly Effective in Vivo Near-Infrared Photothermal Therapy of Cancer. *ACS Nano* **2012**, *6*, 5605–5613.

39. Kalen, J. D. *Positron Emission Tomography: Basic Sciences*; Springer, 2003.

40. Cutler, C. S.; Hennkens, H. M.; Sisay, N.; Huclier-Markai, S.; Jurisson, S. S. Radiometals for Combined Imaging and Therapy. *Chem. Rev.* **2013**, *113*, 858–883.

41. Zhang, Y.; Hong, H.; Engle, J. W.; Bean, J.; Yang, Y.; Leigh, B. R.; Barnhart, T. E.; Cai, W. Positron Emission Tomography Imaging of CD105 Expression with a 64Cu-Labeled Monoclonal Antibody: NOTA Is Superior to DOTA. *PLoS One* **2011**, *6*, E28005.

42. Polášek, M.; Hermann, P.; Peters, J. A.; Geraldes, C. F.; Lukeš, I. PAMAM Dendrimers Conjugated with an Uncharged Gadolinium (III) Chelate with a Fast Water Exchange: The Influence of Chelate Charge on Rotational Dynamics. *Bioconjugate Chem.* **2009**, *20*, 2142–2153.

43. Zhou, M.; Zhang, R.; Huang, M.; Lu, W.; Song, S.; Melancon, M. P.; Tian, M.; Liang, D.; Li, C. A Chelator-Free Multifunctional [64Cu] CuS Nanoparticle Platform for Simultaneous Micro-PET/CT Imaging and Photothermal Ablation Therapy. *J. Am. Chem. Soc.* **2010**, *132*, 15351–15358.

44. Matsumura, Y.; Maeda, H. A New Concept for Macromolecular Therapeutics in Cancer Chemotherapy: Mechanism of Tumoritropic Accumulation of Proteins and the Antitumor Agent Smancs. *Cancer Res.* **1986**, *46*, 6387–6392.

45. Iyer, A. K.; Khaled, G.; Fang, J.; Maeda, H. Exploiting the Enhanced Permeability and Retention Effect for Tumor Targeting. *Drug Discovery Today* **2006**, *11*, 812–818.

46. Moghimi, S. M.; Hunter, C. Capture of Stealth Nanoparticles by the Body's Defences. *Crit. Rev. Ther. Drug Carrier Syst.* **2001**, *18*, 527−550.

47. Rosencwaig, A.; Gersho, A. Theory of the Photoacoustic Effect with Solids. *J. Appl. Phys.* **1976**, *47*, 64–69.

48. Wang, L. V.; Hu, S. Photoacoustic Tomography: In Vivo Imaging from Organelles to Organs. *Science* **2012**, *335*, 1458–1462.

49. Sun, S.; Zeng, H.; Robinson, D. B.; Raoux, S.; Rice, P. M.; Wang, S. X.; Li, G. Monodisperse MFe₂O₄ (M = Fe, Co, Mn) Nanoparticles. *J. Am. Chem. Soc.* **2004**, *126*, 273–279.

50. Cheng, L.; Yang, K.; Li, Y.; Chen, J.; Wang, C.; Shao, M.; Lee, S. T.; Liu, Z. Facile Preparation of Multifunctional Upconversion Nanoprobes for Multimodal Imaging and Dual-Targeted Photothermal Therapy. *Angew. Chem.* **2011**, *123*, 7523–7528.

51. Hong, H.; Yang, K.; Zhang, Y.; Engle, J. W.; Feng, L.; Yang, Y.; Nayak, T. R.; Goel, S.; Bean, J.; Theuer, C. P. In vivo Targeting

and Imaging of Tumor Vasculature with Radiolabeled, Antibody-Conjugated Nanographene. *ACS Nano* **2012**, *6*, 2361–2370.

52. Zhang, Y.; Hong, H.; Severin, G. W.; Engle, J. W.; Yang, Y.; Goel, S.; Nathanson, A. J.; Liu, G.; Nickles, R. J.; Leigh, B. R. ImmunoPET and Near-Infrared Fluorescence Imaging of CD105 Expression Using a Monoclonal Antibody Dual-Labeled with 89Zr and IRDye 800CW. *Am. J. Transl. Res.* **2012**, *4*, 333–346.

53. Hong, H.; Zhang, Y.; Severin, G. W.; Yang, Y.; Engle, J. W.; Niu, G.; Nickles, R. J.; Chen, X.; Leigh, B. R.; Barnhart, T. E. Multimodality Imaging of Breast Cancer Experimental Lung Metastasis with Bioluminescence and a Monoclonal Antibody Dual-Labeled with 89Zr and IRDye 800CW. *Mol. Pharmaceutics* **2012**, *9*, 2339–2349.

54. Shi, S.; Yang, K.; Hong, H.; Valdovinos, H. F.; Nayak, T. R.; Zhang, Y.; Theuer, C. P.; Barnhart, T. E.; Liu, Z.; Cai, W. Tumor Vasculature Targeting and Imaging in Living Mice with Reduced Graphene Oxide. *Biomaterials* **2013**, *34*, 3002–3009.